Atmos. Chem. Phys. Discuss., 5, 11377–11412, 2005
www.atmos-chem-phys.org/acpd/5/11377/
SRef-ID: 1680-7375/acpd/2005-5-11377
European Geosciences Union

Atmospheric Chemistry and Physics Discussions

Small-scale gravity waves in ER-2 MMS/MTP wind and temperature measurements during CRYSTAL-FACE

L. Wang[1], M. J. Alexander[1], T. P. Bui[2], and M. J. Mahoney[3]

[1]Colorado Research Associates Division, NorthWest Research Associates, Inc., Boulder, CO 80301, USA
[2]NASA Ames Research Center, Moffett, CA 94035, USA
[3]Jet Propulsion Laboratory, California Institute of Technology, Pasadena, CA 91109, USA

Received: 10 October 2005 – Accepted: 2 November 2005 – Published: 10 November 2005

Correspondence to: L. Wang (lwang@cora.nwra.com)

Abstract

ER-2 MMS and MTP wind and temperature measurements during the CRYSTAL-FACE campaign in July 2002 were analyzed to retrieve information on small scale gravity waves (GWs) at aircraft's flight level. For a given flight segment, the S-transform was used to search for and identify small horizontal scale GW events, and to estimate the apparent horizontal wavelengths of the events. The horizontal propagation directions of the events were determined using the Stokes parameters method combined with the cross S-transform analysis. The MTP temperature gradient method was used to determine the vertical wavelengths of the events. GW momentum fluxes were calculated from the cross S-transform. Other wave parameters such as intrinsic frequencies were calculated using the GW dispersion relation. More than 100 GW events were identified. They were generally short horizontal scale and high frequency waves with λ_z of ~5 km and λ_h generally shorter than 20 km. Their intrinsic propagation directions were predominantly toward the east, whereas their ground-based propagation directions were primarily toward the west. Among the events, ~20% of them had very short horizontal wavelength (<10 km), very high intrinsic frequency ($\omega/N \geq 0.8$), and relatively small momentum fluxes, and thus they were likely trapped in the lower stratosphere. The averaged magnitude of vertical flux of horizontal momentum was ~0.026 kg m^{-1} s^{-2}, and the maximum magnitude was ~0.13 kg m^{-1} s^{-2}.

Using the estimated GW parameters and the background winds and stabilities from the NCAR/NCEP reanalysis data, we were able to trace the sources of the events using a simple reverse ray-tracing. More than 70% of the events were traced back to convective sources in the troposphere, and the sources were generally located upstream to the events. Finally, a probability density function of GW cooling rates was obtained in this study, which may be used in cirrus cloud models.

ACPD

5, 11377–11412, 2005

1. Introduction

GWs are commonly observed at all levels in the atmosphere. Their role in the global circulation became widely appreciated twenty years ago when their effects were first parameterized in global circulation models (Palmer et al., 1986; McFarlane, 1987). The wave effects on the global circulation are quite sensitive to the properties of the gravity waves, e.g. their phase speeds, horizontal and vertical wavelengths, and the momentum flux they carry (e.g. Holton, 1982; Alexander and Dunkerton, 1999). Hence, numerous observational studies have attempted to quantify these properties (see Fritts and Alexander, 2003). Most data sets do not provide enough information to quantify all the needed wave properties (Bacmeister, et al., 1990a, b; Pfister et al., 1993; Alexander and Pfister, 1995; Bacmeister et al., 1996; Alexander et al., 2000), but measurements from the ER-2 aircraft platform during the Cirrus Regional Study of Tropical Anvils and Cirrus Layers – Floria Area Cirrus Experiment do (CRYSTAL-FACE (Jensen et al., 2004).

Convection is one of the globally important sources of gravity waves, and the CRYSTAL-FACE flights in the vicinity of subtropical and tropical deep convection provide a wealth of data on waves from this source. Simultaneous measurements of 3-dimensional vector winds from the Meteorological Measurement System (MMS) and vertical temperature gradients from the Microwave Temperature Profiler (MTP) can be combined to fully characterize the waves sampled by the ER-2 in the lower stratosphere.

One motivation of this study is to provide observational constraints for parameterizations developed to describe the effects of convectively generated GWs (Chun and Baik, 1998, 2002; Beres et al., 2004). The simplifying assumptions in these parameterizations are poorly validated to date. The location of the CRYSTAL-FACE campaign was south Florida and the Caribbean region where convection is believed to be the major source of GWs. We hope the detailed analysis of GW properties in this study will help to validate these parameterization schemes.

ACPD
5, 11377–11412, 2005

Recent studies show that GWs in the upper troposphere and lower stratosphere were found to influence the formation of high and cold cirrus clouds considerably (Jensen et al., 2001; Jensen and Pfister, 2004; Haag and Kärcher, 2004; Jensen et al., 2005) through wave induced temperature oscillations. Cirrus clouds, especially those in the tropical tropopause layer (TTL), play important roles in the Earth's radiation budget and the stratospheric water vapor budget as cirrus formed in situ within the TTL can effectively dehydrate air entering the stratosphere (Jensen et al., 2001; Jensen and Pfister, 2004). Tropical cirrus clouds also play a significant role in stratospheric chemistry by affecting the stratospheric humidity (Solomon et al., 1986). One of the main challenges to predict the effects of cirrus clouds on stratospheric water vapor concentrations, however, is to predict the temperature in the TTL, which is modulated considerably by GWs (Jensen and Pfister, 2004). The focus of this study is to analyze in detail the properties of short horizontal scale GWs the South Florida region from MMS and MTP wind and temperature measurements obtained on board the ER-2 aircraft. We hope the results of this study may be helpful to numerical studies of TTL cirrus clouds.

The paper is organized as follows. Section 2 describes the wind and temperature data used in this study. Section 3 describes the procedures to identify GW events and to estimate GW parameters such as wavelength, propagation direction, and momentum flux of the events. It also shows the statistics of the parameters derived. Section 4 investigates the sources of the wave events. Discussions are given in Sect. 5. In the end, summary and conclusions are given.

2. Data

During the CRYSTAL-FACE campaign in July 2002, multiple sorties of NASA's ER-2 aircraft were carried out over the southern Florida and Caribbean region (12.4–29.9° N, 273.1–283.0° E) to measure atmospheric properties in the lower stratosphere and upper troposphere. The aircraft flew at ~20 km with a cruise speed of ~200 ms^{-1}. There were 10 flights in total and Table 1 shows the time information of the flights. Each flight

ACPD
5, 11377–11412, 2005

started from either late morning or early afternoon and ended in late afternoon (in local time). Each flight mission lasted ∼6–7 h, and covered a total horizontal distance of ∼4000–5000 km. Figure 1 shows, for example, the ER-2 flight track during 7 July 2002 between 16:01 and 22:39 UTC.

Among the instruments aboard the ER2 aircraft, meteorological measurement system (MMS) measured in situ winds, temperature, and pressure (Scott et al., 1990), whereas microwave temperature profiler (MTP) measured vertical temperature profiles along the flight path by microwave remote sensing (Denning et al., 1989). The precisions of MMS winds, temperature, and pressure were 0.1 ms^{-1}, 0.1°K, and 0.1 mb, respectively. The precision of MTP temperature was ∼0.25 K at the flight level. The sampling rate of MMS was 1 Hz. Given the ER-2 speed at ∼200 ms^{-1}, the horizontal resolution of MMS measurements was therefore 0.2 km. The sampling rate of MTP was 0.1 Hz. The horizontal resolution of MTP temperature depended on the molecular oxygen absorption coefficient, and it was 1.3–2.5 km. The vertical profile of MTP temperature generally extended ∼9 km above and below the flight altitude for the measurements analyzed in this study. The vertical resolution of MTP temperature profile varies with distance from the aircraft, being ∼0.1 km at flight level and ∼2 km at 5 km from flight level.

To facilitate gravity wave (GW) analyses, we first divided each flight into flight segments (or legs) within which the flight altitude was nearly constant at ∼20 km and the flight path was nearly straight so as to avoid turns and rapid ascents and descents of the aircraft. Also, we required that the length of each segment be no shorter than 50 km. The highlighted portion of the flight track in Fig. 1 shows an example of such a flight segment. In total, 136 flight segments were selected. Their horizontal spans ranged from ∼50 to ∼1100 km, with the majority having a value of ∼200 km. The flights on 9 and 26 July were exceptional in that they contained a few very long flight segments (∼1000 km or longer) which reached as far south as ∼12.4° N and deep into the Caribbean. The orientations of the flight segments were somewhat anisotropic in the sense that more segments were aligned zonally than meridionally.

ACPD
5, 11377–11412, 2005

Figure 2 shows the MMS wind and temperature for the flight segment highlighted in Fig. 1. Overplotted on the MMS temperature is the MTP temperature at the flight altitude. The raw data were interpolated to a regular grid interval of 0.2 and 2 km for MMS and MTP data, respectively. The MMS and MTP temperatures generally agreed very well, though the former had a better temporal resolution. Figure 3 shows the contour (flight distance vs. altitude) of the corresponding MTP temperature linearly detrended in the vertical. In this plot, the MTP raw temperature was interpolated bilinearly to a regular distance grid interval of 2 km and a regular vertical grid interval of 0.5 km. Note that localized wavy structures are clearly seen in Figs. 2 and 3, especially for horizontal winds and temperatures. It is assumed in this study that these wavy structures are GW events (or packets).

In the next section, we will describe the procedure to identify GW events from the flight segments in a more quantitative way, and will estimate GW parameters including wavelengths, horizontal propagation directions, and momentum fluxes for such events.

3. GW parameters

3.1. GW event and apparent horizontal wavelength

As mentioned in the previous section, GW packets were clearly seen in the horizontal wind and temperature data for the flight segment shown in Fig. 1. To determine the locations and amplitudes of these wave packets quantitatively, we applied the S-transform to the MMS wind and temperature along the flight segment. The S-transform (Stockwell et al., 1996) is a continuous wavelet transform (*CWT*) whose basis functions are formed as the product of a Gaussian envelope and sine/cosine functions. The *CWT* $W_h(\xi, d)$ of a function $h(x)$ is defined by

$$W_h\left(\xi, \lambda_h'\right) = \int_{-\infty}^{\infty} h(x) w(x - \xi, \lambda_h') dx \quad (1)$$

ACPD
5, 11377–11412, 2005

where x is horizontal distance, λ_h' is the apparent horizontal wavelength. The mother wavelet w is defined as

$$w(x,k) = \frac{|k|}{\sqrt{2\pi}} e^{-\frac{x^2k^2}{2}} e^{-i2\pi kx} \quad (2)$$

where k is inverse of λ_h', i.e., the apparent horizontal wavenumber, and i is the imaginary unit. The S-transform method has already been applied to geophysical data and has proved to be useful in estimating wave perturbation amplitudes and phase information (e.g., Stockwell and Lowe, 2001; Wang et al., 2005a[1]).

Figure 4 shows contours of horizontal distance vs. apparent horizontal wavelength λ_h' of wave amplitudes in winds and temperatures from the S-transform for the regularly gridded MMS data shown in Fig. 2. The locations and amplitudes of GW packets are clearly seen in the contour plot. Notably, there was a strong wave signal with a dominant λ_h' of ~63 km for both temperature and zonal wind between 1630 and 1750 km flight distance. The S-transform detected another wave packet with a shorter λ_h' (~21 km), occurring between 1630 and 1750 km flight distance. It showed up in all the variables, although less clear in w in comparison to the others. In this study, we defined a GW event when coherent wave perturbations showed up in both temperature and at least one component of horizontal winds at the same flight distance and at the same λ_h'. Also, we only focused on signals with dominant λ_h' no shorter than 5 km. In Fig. 4, the dashed lines indicate the GW events thus identified for this particular flight segment.

In total, 138 such wave events were identified from the flight segments available. Figure 5 shows the histogram of λ_h' and the angular distribution of the flight directions of the events. Most of the events had a dominant λ_h' 10–20 km. Also, the average wave amplitudes were ~0.69 ms^{-1}, 0.75 ms^{-1}, 0.35 ms^{-1}, and 0.39 K, for u, v, w, and T,

[1]Wang, L., Fritts, D. C., Williams, B. P., Goldberg, R. A., Schmidlin, F. J., and Blum, U.: Gravity waves in the middle atmosphere during the MaCWAVE winter campaign: Evidence of mountain wave critical level encounters, Ann. Geophys., submitted, 2005a.

respectively (not shown). It is worth noting that coherent wave perturbations showed up in both MMS T and w for 72% of the GW events. Statistically, coherence between MMS w and T was best for GW events with short λ_h', and it worsened as λ_h' increased. Such coherence held up for λ_h' as long as ~90 km (Fig. 5). Note that λ_h' is related to the true GW horizontal wavelength λ_h by $\lambda_h = \lambda_h' \cos\theta$, where θ is the angle between the flight direction and the GW horizontal propagation direction ϕ, which will be discussed in the next subsection.

3.2. Vertical wavelength and horizontal propagation direction

The dominant vertical wavelengths λ_z of the GW events identified above were estimated using the MTP vertical temperature gradient as follows:

$$\lambda_z = 2\pi \left| \frac{iT'}{dT'/dz} \right| \sim 2\pi \frac{\sigma(T')}{\sigma(dT'/dz)} \tag{3}$$

where T' is the GW perturbation from the MTP temperature, i is the imaginary unit, and $\sigma(T')$ is the standard deviation of T', i.e.,

$$\sigma(T') = \sqrt{\frac{1}{n-1} \sum_{i=1}^{n} (T_i' - \overline{T'})^2} \tag{4}$$

We used the standard deviation because single realizations of ratio $T'/(dT'/dz)$ can be singular while the ratio of the standard deviations gives the correct result for a theoretical monochromatic wave. T' was derived from linearly detrending the MTP temperature for each event. To increase the statistical confidence of the standard deviations in Eq. (3), in practice, we calculated λ_z for only those events which had at least 6 MTP temperature measurements available. For the two GW events identified in Fig. 4, λ_z was 7.2 and 8.1 km for the ones with longer and shorter λ_h', respectively. Note that three of the events (two on 3 July and one on 13 July) had too few MTP measurements to determine their λ_z.

According to linear GW theory, the (intrinsic) horizontal propagation direction of a GW ϕ is aligned with the major axis of the wind perturbation hodograph (Gossard and Hooke, 1975). Such a property of GWs has been used in previous studies to estimate ϕ from vertical profiles of winds and temperatures with the aid of the Stokes parameter method or hodographic analysis (e.g., Zink and Vincent, 2000; Wang et al., 2005a[1]). Similar to Zink and Vincent (2001), we derived ϕ from GW wind and temperature perturbations along flight track using the Stokes-parameter technique (e.g., Eckermann and Vincent, 1989). Briefly, for a monochromatic GW, the relevant Stokes parameters are defined as

$$D = \tilde{u}^2 - \tilde{v}^2 \tag{5}$$

$$P = 2\tilde{u}\tilde{v}\cos\delta \tag{6}$$

where $\tilde{u}$ and $\tilde{v}$ are the amplitudes of u and v, respectively, and δ is $(\Phi_v - \Phi_u)$, i.e., the phase difference between v and u. In optical terms, D is the throughput anisotropy parameter, and P is the linear polarization parameter. The major axis orientation ϕ' of GW wind perturbation hodograph is given by (Kraus, 1966)

$$\phi' = \frac{1}{2}\arctan\left(\frac{P}{D}\right) \tag{7}$$

In practice, $\tilde{u}$ and $\tilde{v}$ were calculated directly from the S-transform amplitudes of the MMS winds for the GW events identified. The phase difference δ was calculated by performing a cross-S-transform analysis (cross ST) of the MMS winds in analogy with cross-spectral analysis using the Fourier transform. The cross ST of two time series $h(x)$ and $g(x)$ is defined as

$$W_h(\xi, k)\{W_g(\xi, k)\}^* \tag{8}$$

where $\{W_g(\xi, k)\}^*$ is the complex conjugate of $W_g(\xi, k)$. The phase of the cross ST can be shown to be equivalent to the phase difference between $g(x)$ and $h(x)$, $\Phi(\xi, k)_g - \Phi(\xi, k)_h$.

There is a 180° ambiguity of ϕ', however, since ϕ' can only vary between $[-\pi/2, \pi/2]$. To solve such an ambiguity, we used the additional information of temperature. It can be shown that the phase difference between T and u along the flight track is (see the Appendix)

$$\Phi_T - \Phi_u = \arctan\left(\frac{\tilde{v}\sin(\phi)\sin(\delta)}{\tilde{u}\cos(\phi) + \tilde{v}\sin(\phi)\cos(\delta)}\right) - \frac{\pi}{2} \quad (9)$$

where again, in practice, $(\Phi_T - \Phi_u)$ was calculated using the cross ST. ϕ is either ϕ' or $(\phi' + \pi)$ depending on which one satisfies Eq. (9) more closely.

With ϕ derived, the true dominant horizontal wavelength λ_h is simply the apparent dominant horizontal scale λ'_h multiplied by the cosine of the angle between ϕ and the flight path, as mentioned in the previous subsection. Other wave parameters such as intrinsic frequency $\hat{\omega}$, group velocity, and intrinsic phase speed, were determined from the GW dispersion relation. For the two GW events identified in Fig. 4, ϕ, λ_h, and $\hat{\omega}$ are ~352°, 44.6 km, and 51f (=0.0032 s^{-1}, f is the Coriolis parameter) for the event with longer λ'_h and 154°, 18.7 km, and 126f (=0.0079 s^{-1},), respectively, for the event with shorter λ'_h, respectively, where ϕ is measured counter clockwise from the East. For the two events, the ratios of Brunt-Väisälä frequency N derived from the NCAR/NCEP reanalysis data and f were ~319. Note that $\hat{\omega}$ can also be derived from the Stokes parameter method since $\hat{\omega}/f$ is equal to the GW perturbation ellipse axial ratio which can be related to some Stoke parameters (e.g., Eckermann and Vincent, 1989). We chose not to use this approach since we were mostly dealing with short horizontal scale and high intrinsic frequency waves, for which noise in the data makes this approach prone to larger errors.

Figure 6 shows the histogram of λ_z and the angular distribution of ϕ for the GW events. The waves generally had λ_z of ~5 km and they propagated predominantly eastward. There also appeared to be a northward bias in ϕ. The waves were generally short horizontal scale and high intrinsic frequency with λ_h generally shorter than 20 km and $\hat{\omega}$ higher than 13 f (not shown). The averaged intrinsic phase speed and

ACPD
5, 11377–11412, 2005

magnitude of ground-based group velocity were ∼13 and 18 ms^{-1}, respectively (not shown). Finally, note that since λ_z was undetermined for three of the events, $\hat{\omega}/f$, intrinsic phase speed and ground-based group velocity were also undetermined for them.

3.3. Momentum flux

Assuming a locally horizontally homogeneous atmosphere, the GW induced force on the background wind $\left(\overline{X}, \overline{Y}\right)$ is related to the vertical gradient of the vertical flux of horizontal momentum $\left(F_{px}, F_{py}\right)$ (or simply put, momentum flux) by

$$\left(\overline{X}, \overline{Y}\right) = -\frac{\epsilon}{\overline{\rho}} \frac{\partial}{\partial z} \left(F_{px}, F_{py}\right) \tag{10}$$

where ϵ is an intermittency factor (Alexander and Dunkerton, 1999), $\overline{\rho}$ is the background density, and $\left(F_{px}, F_{py}\right)$ is defined as

$$\left(F_{px}, F_{py}\right) = \overline{\rho} \left[\left(1 - f^2/\hat{\omega}^2\right) \left(\overline{u'w'}, \overline{v'w'}\right)\right] \tag{11}$$

Hence, momentum fluxes are very important quantities which are related directly to the effects of GWs on the background atmosphere. With MMS vertical velocity available, we were able to calculate the fluxes directly. We estimated momentum fluxes for the GW events using the S-transform and cross ST analysis. For a monochromatic GW, Eq. (11) leads to

$$F_{px} = \frac{1}{2}\overline{\rho} \left(1 - f^2/\hat{\omega}^2\right) \tilde{u}\tilde{w}(\Phi_w - \Phi_u) \tag{12}$$

$$F_{py} = \frac{1}{2}\overline{\rho} \left(1 - f^2/\hat{\omega}^2\right) \tilde{v}\tilde{w}(\Phi_w - \Phi_v) \tag{13}$$

In practice, $\tilde{u}\tilde{w}$, $\tilde{v}\tilde{w}$, $(\Phi_w - \Phi_u)$, and $(\Phi_w - \Phi_v)$ were calculated using the cross ST for each event. $\overline{\rho}$ was calculated from the event mean density which was derived

ACPD
5, 11377–11412, 2005

from MMS T and pressure. $\hat{\omega}$ was already estimated from the GW dispersion relation as described in the previous subsection. Since a GW event was generally not purely monochromatic, the contributions from horizontal wavelengths adjacent to the dominant horizontal wavelength λ_h' were added to the value at λ_h' to produce the total momentum flux of the wave event. For the two events identified in Fig. 4, (F_{px}, F_{py}) was ∼(0.008, 0) and (−0.06, −0.004) kg m^{-1} s^{-2} for the one with longer λ_h' and the one with shorter λ_h', respectively. Figure 7 shows the histogram of the magnitudes of momentum flux $\sqrt{F_{px}^2+F_{py}^2}$ for the GW events identified in this study. The averaged magnitude was ∼0.026 kg m^{-1} s^{-2}, and the maximum magnitude was ∼0.13 kg m^{-1} s^{-2}. These values generally agree with previous estimates of GW momentum fluxes in the lower stratosphere over convection (e.g., Alexander and Pfister, 1995; Alexander et al., 2000).

Note that GWs' horizontal propagation directions can also be derived from the momentum fluxes (F_{px}, F_{py}), as $\tan(\phi)=F_{py}/F_{px}$. We compared the propagation directions derived using the flux method with those from the Stokes parameter method, and found that they agreed for most events. Specifically, their difference was less than 30° for ∼81% of the events, and the angular distribution of horizontal propagation directions derived using the flux method also showed the eastward bias, as did ϕ. Large discrepancies existed for ∼19% of the events. We will discuss potential reasons for these discrepancies in Sect. 5.

4. Wave sources

To investigate the sources of the GW events, we ray-traced each event back using a simple group velocity method, i.e., $d\boldsymbol{r}/dt=\boldsymbol{C_g}$, where $\boldsymbol{r}$ is the position vector of the event and $\boldsymbol{C_g}$ is the 3-D group velocity. The initial $\boldsymbol{C_g}$ was calculated using the wave parameters derived in the previous section and the background winds and stabilities from the four-times daily NCAR/NCEP reanalysis data. For the subsequent time steps,

ACPD
5, 11377–11412, 2005

C_g was calculated from the ground-based frequency ω, and horizontal wavenumbers k, l which were assumed to be constant during the ray-tracing. The temporally and spatially varying background u, v, N were estimated from interpolating the reanalysis data to the current time and location of each event. The reverse ray-tracing was terminated when any of the following conditions was met: the tracing time reached 3 h, the ray reached the ground, or the wave was refracted so much that its intrinsic frequency was beyond the possible range of a propagating GW, i.e., being smaller than f or larger than N. The horizontal and 3-hour-temporal variations of the background fields were generally much smaller in comparison to the vertical variations in the tropical and subtropical region, so the assumption of constant k, l was valid.

The trajectory of each event was compared to the NASA Langley NEXRAD radar reflectivity images which were available every 10 min. As an example, Fig. 8 shows the NEXRAD radar reflectivity image on 7 July 2002 17:20 UTC. The gray line is the ER-2 flight track on that day. The solid red line denotes the GW event with the longer λ_h' shown in Fig. 4. The event was detected at flight level at ~18:20 UTC. The solid pink lines denote the trajectories at both ends of the event reversely ray-traced 1 h back to 17:20 UTC. The dotted red line connects the end points of the trajectories and indicates where the wave event could have been 1 h earlier. The altitude corresponding to the dotted red line was ~7.5 km in the mid troposphere for both end points. It is evident from Fig. 8 that the wave event was located over a convectively active region in the troposphere 1 h before it was observed in the lower stratosphere by the ER-2 aircraft, implying that the source of the event was most likely the strong convection in the troposphere at ~(25.5° N, 81.3° W).

Of the 135 events for which we conducted ray-tracing (ray-tracing was not possible for the remaining 3 events since their λ_z could not be determined due to the gap in MTP temperature data), ~76% of them were traced back to convective sources below 13 km in the troposphere (the average tropopause height was ~15 km). This is not surprising since convection was expected to be the major source of GWs for these CRYSTAL-FACE flights.

For those GW events which could not be traced back to convective sources in the troposphere, most of them had short λ_h and high original $\hat{\omega}$ in comparison to those found to be associated with convective sources. Their $\hat{\omega}$ exceeded N above 13 km.

Figure 9 shows the angular distribution of source to event directions for those events related to convective sources (102 in total), and the scatter plot of their background winds at flight level. The source to event direction was defined as the direction from the mid-point of each event to the convective sources we identified. Most of the sources were located upstream to the events.

5. Discussions

As shown in Fig. 5, coherent wave perturbations showed up in both MMS T and w for 72% of the GW events, and the coherence was generally better for shorter λ_h' (and λ_h as well, not shown). The GW polarization relation between vertical velocity and temperature is

$$\tilde{w} = \frac{i\hat{\omega}g}{N^2}\tilde{T}' \sim \frac{i\lambda_z g}{N\lambda_h}\tilde{T}' \tag{14}$$

where g is the gravitational acceleration, $\tilde{T}'$ is the GW perturbation temperature amplitude divided by the background temperature, and other notations were defined previously. The approximation in Eq. (14) follows from the GW dispersion relation. Evidently, for a given $\tilde{T}'$, a GW with longer λ_h has smaller $\tilde{w}$, and vice versa. Thus, we expect that the coherence between T and w to deteriorate for longer horizontal scale GWs. In general, for longer horizontal scale waves, higher signal to noise ratio for vertical velocity measurements is needed as $\tilde{w}$ gets smaller.

Most of the wave events identified in this study were found to be short horizontal scale and high intrinsic frequency GWs, as mentioned in Sect. 3. In fact, such waves are prone to be trapped in the atmosphere (Isler et al., 1997; Swenson et al., 2000; Marks and Eckermann, 1995), and the trapped waves carry no momentum flux. To see

how many of the waves events were trapped or evanescent waves instead of propagating waves, we show on the left panel of Fig. 10 the percentage of GW events within each λ_h and $\hat{\omega}/N$ bin. 135 events were included in the plot. Bins are blank if no GW events fall into them. The right panel of Fig. 10 shows the corresponding bin-averaged magnitudes of momentum flux of the GW events. Evidently, most of the events had $\hat{\omega}/N$ equal to or larger than 0.1 and λ_h shorter than 20 km. In contrast, GWs observed from radiosondes (e.g., Vincent and Alexander, 2000; Wang, 2003; Wang et al., 2005b), generally had $\hat{\omega}/N$ less than 0.01 and λ_h of ~1000 km or longer at similar latitudes. Generally, shorter horizontal scale GWs had larger momentum fluxes and the largest fluxes occurred for GWs with λ_h less than 10 km and $\hat{\omega}/N$ between 0.4 and 0.5. Interestingly, all the GW events which had $\hat{\omega}/N$ equal to or larger than 0.8 had λ_h shorter than 10 km, and their momentum fluxs were considerably smaller than those GWs with similar λ_h but relatively lower $\hat{\omega}/N$, thus suggesting that these very high frequency GWs were likely trapped waves. In total, there were 27 such trapped GW events (i.e., 20% of the 135 events whose $\hat{\omega}/N$ were determined). None of the reverse ray-traces of these very high intrinsic frequency waves could extend down to the troposphere below 13 km (not shown).

As mentioned in section 3, the intrinsic horizontal propagation directions of the events were predominantly eastward (Fig. 6). Similar anisotropies of GW horizontal propagations have been observed in previous studies in the tropical and subtropical lower stratosphere (e.g., Vincent and Alexander, 2000; Wang, 2003). As mentioned above, our results are distinct from the previous studies in that the GWs examined in this study were short horizontal scale and high intrinsic frequency GWs, whereas the previous studies as referenced here focused on long horizontal scale and low intrinsic frequency inertio GWs.

Figure 11 shows the typical background wind and temperature from 3–5 times daily high vertical resolution radiosonde observations conducted during the CRYSTAL-FACE campaign. They were derived from binning the raw balloon data from four south Florida stations (Key West, FL, 24.5° N, 81.8° W; Miami, FL, 25.8° N, 80.4° W; PARSL mobile

ACPD
5, 11377–11412, 2005

facility, 25.8° N, 81.4° W; and Tampa Bay Area, FL, 27.7° N, 82.4° W) during July 2002. The error bars indicate the magnitude of the standard deviation for each bin. Zonal winds were generally toward the west. They were very weak in the lower troposphere and increased to $\sim -16\,\mathrm{ms}^{-1}$ at 20 km. Meridional winds were very weak with absolute values less than $4\,\mathrm{ms}^{-1}$ throughout the troposphere and lower stratosphere. The tropopause was well defined and was located at ~15 km.

Note that the prevalent westward background winds offset the eastward anisotropy of intrinsic horizontal propagation directions ϕ so that the ground-based propagation directions were actually predominantly westward at slow ground-based phase speeds (not shown). This is consistent with Fig. 9 which showed that that sources were mostly located upstream to the events.

The anisotropy of GW intrinsic horizontal propagation directions (Fig. 6) may be caused largely by the anisotropy of the wave sources, as Alexander and Vincent (2000) and Wang (2003) found out for the low intrinsic frequency waves they studied from balloon data, though background wind filtering effect definitely played a role in modifying the morphology of the waves that we observed. It is difficult to determine the relative importance of the two factors without further analysis and additional data.

Finally, as mentioned in the introduction, GWs play a significant role in the dynamics of cirrus cloud formation in the TTL region. One way to quantify their effects in cirrus cloud models is to calculate the cooling rate due to GWs by $\hat{\omega}\tilde{T}$ (Jensen and Pfister, 2004), where $\tilde{T}$ is the GW temperature perturbation amplitude. In fact, $\hat{\omega}\tilde{T}$ is readily available from this study. Figure 12 shows the probability of observing a GW event with a certain cooling rate. The probability was calculated from the ratio of the sum of the horizontal extents of the GW events (e.g., the lengths of the dashed lines in Fig. 4) having cooling rates within a certain range and the total distances of all the flight segments examined in this study. Overall, there was a 32% chance of observing a GW event in ER-2 flights during CRYSTAL-FACE, so the sum of probabilities in Fig. 12 is 0.32. Most events had cooling rates less than 22 K/h.

ACPD
5, 11377–11412, 2005

6. Conclusions

ER-2 MMS and MTP wind and temperature measurements during CRYSTAL-FACE in July 2002 were analyzed to investigate short horizontal scale GWs at flight altitude (~20 km). There were 10 ER-2 sorties over the southern Florida and the Caribbean region during the campaign (Table 1).

To facilitate GW analysis, we divided each flight into flight segments (or flight legs) within which the flight altitude was nearly constant at ~20 km and the flight path was nearly straight so as to avoid turns and rapid ascents and descents of the aircraft. Also, we required that the length of each segment be no shorter than 50 km. 136 such flight segments were selected. We then applied the S-transform (a wavelet transform) to each flight segment to identify GW events in the segment, if there were any. A GW event was identified if coherent wave perturbations showed up in both temperature T and at least one component of horizontal winds at the same flight distance range and at the same apparent horizontal wavelength λ_h' (Fig. 4). We only focused on signals with dominant λ_h' no shorter than 5 km. 138 such wave events were identified. Meantime, we found that coherent wave perturbations showed up in both T and vertical velocity w for 72% of the GW events (Fig. 5). The shorter the λ_h' was, the better the correspondence between w and T was, and such a coherence held up for λ_h' up to ~90 km.

The dominant vertical wavelengths λ_z of the GW events were estimated using the vertical gradient of MTP temperature perturbations. The horizontal propagation directions ϕ were estimated from MMS horizontal winds using the Stokes parameter method with the aid of the cross S-transform. In addition, MMS temperature was used to solve the 180° ambiguity of ϕ. The true horizontal wavelengths λ_h were calculated from λ_h' and the angles between ϕ and the flight directions of the events. Other wave parameters such as intrinsic frequencies $\hat{\omega}$, group velocities, and intrinsic phase speeds, were determined from the GW dispersion relation.

The wave events were found to be generally short horizontal scale and high frequency GWs with λ_z of ~5 km, λ_h generally shorter than 20 km, and $\hat{\omega}$ higher than 13

ACPD
5, 11377–11412, 2005

f, and they propagated predominantly eastward, i.e., being opposite to the background winds (Fig. 6). The averaged intrinsic phase speed and magnitude of group velocity were ~13 and 18 ms^{-1}, respectively.

Vertical fluxes of horizontal momentum of the GW events (F_{px}, F_{py}) were calculated from the MMS winds using the cross S-transform. The averaged momentum flux magnitude was ~0.026 kg m^{-1} s^{-2}, and the maximum magnitude was ~0.13 kg m^{-1} s^{-2} (Fig. 7). We also calculated the horizontal propagation directions of the events using the estimated fluxes and found the results generally agreeing with those from the Stokes parameters method.

We reverse ray-traced the GW events using their 3-D group velocities and the background winds and stabilities from the NCAR/NCEP reanalysis data to trace their sources in the troposphere. The 3-D group velocities were calculated by assuming that the horizontal wavelengths of the events remained constant. The trajectories of the events were compared to the NASA Langley NEXRAD radar reflectivity images available every 10 min during July 2002. Of the 135 events for which we were able to perform ray-tracing, ~76% of them were traced back to convective sources below 13 km in the troposphere and most of the sources were located upstream to the events (Fig. 9).

Among the 135 events that we were able to determine $\hat{\omega}/N$, 20% of them had very short horizontal wavelength (<10 km), very high intrinsic frequency ($\hat{\omega}/N \geq 0.8$), and relatively small momentum fluxes, and thus were likely trapped or evanescent waves.

Finally, a probability density function of GW cooling rates was derived from the GW temperature perturbation amplitudes, intrinsic frequencies, the horizontal extents of the events, and the total distances of flight segments during CRYSTAL-FACE. Such information can be used in cirrus cloud model studies.

ACPD
5, 11377–11412, 2005

Appendix A

Solving the 180° ambiguity of GW horizontal propagation direction derived from the Stokes parameters method

GW perturbation winds and temperature can be written as

$$u' \equiv \tilde{u}\cos(\Phi_u) \tag{A1}$$

$$v' \equiv \tilde{v}\cos(\Phi_v) \tag{A2}$$

$$\hat{T}' \equiv \tilde{T}\cos(\Phi_T) \tag{A3}$$

Let $u'_{\parallel}$ designate the horizontal perturbation velocity parallel to the wave vector (or the propagation direction) and let ϕ designate the horizontal propagation direction, it follows that

$$\begin{aligned} u'_{\parallel} &\equiv \tilde{u}_{\parallel}\cos(\Phi_{u_{\parallel}}) \\ &= u'\cos(\phi) + v'\sin(\phi) \\ &= \tilde{u}\cos(\Phi_u)\cos(\phi) + \tilde{v}\cos(\Phi_v)\sin(\phi) \end{aligned} \tag{A4}$$

Let $A \equiv \tilde{u}\cos(\phi)$, $B \equiv \tilde{v}\sin(\phi)$, and $\delta\phi \equiv \Phi_v - \Phi_u$, Eq. (A4) leads to

$$\begin{aligned} u'_{\parallel} &= A\cos(\Phi_u) + B\cos(\Phi_u + \delta\phi) \\ &= A\cos(\Phi_u) + B\cos(\Phi_u)\cos(\delta\phi) - B\sin(\Phi_u)\sin(\delta\phi) \\ &= [A + B\cos(\delta\phi)]\cos(\Phi_u) - B\sin(\delta\phi)\sin(\Phi_u) \\ &= C_1\cos(\Phi_u) - C_2\sin(\Phi_u) \end{aligned} \tag{A5}$$

where $C_1 \equiv A + B\cos(\delta\phi)$ and $C_2 \equiv B\sin(\delta\phi)$. Define

$$\alpha \equiv \arctan(C_2, C_1) \tag{A6}$$

ACPD
5, 11377–11412, 2005

Equation (A5) can be rewritten as

$$u'_{\|} = \sqrt{{C_1}^2 + {C_2}^2}\,[\cos(\alpha)\cos(\Phi_u) - \sin(\alpha)\sin(\Phi_u)]$$

$$= \sqrt{{C_1}^2 + {C_2}^2}\cos(\Phi_u + \alpha) \quad \text{(A7)}$$

which leads to

$$\tilde{u_{\|}} = \sqrt{{C_1}^2 + {C_2}^2} \quad \text{(A8)}$$

and

$$\Phi_{u_{\|}} = \Phi_u + \alpha \quad \text{(A9)}$$

The relevant GW polarization relation in the Boussinesq approximation is

$$\hat{T}' = i\frac{N^2}{g\hat{\omega}}\frac{k_h}{m}u'_{\|} \quad \text{(A10)}$$

Since m<0 and k_h>0 by convention, and $-i\cos(x)=\cos(x-\frac{\pi}{2})$, thus

$$\Phi_T = \Phi_{u_{\|}} - \frac{\pi}{2} \quad \text{(A11)}$$

Equations (A9) and (A11) lead to

$$\Phi_T - \Phi_u - \alpha + \frac{\pi}{2} = 0 \quad \text{(A12)}$$

Note that ϕ can be either ϕ' or $\phi'+\pi$, depending on the phase relationship between winds and temperature, where ϕ' is the orientation of the major axis of GW perturbation hodograph as derived using the Stokes parameter method. Equation (A12) is used to solve the 180° ambiguity of ϕ.

Acknowledgements. The authors are grateful to E. Jensen for insightful discussions on this paper. The research by L. Wang and M. J. Alexander was supported by the National Science Foundation Physical & Dynamical Meteorology Program grant ATM-0234230. Work performed by M. J. Mahoney at the Jet Propulsion Laboratory, California Institute of Technology, was done under contract with the National Aeronautics and Space Administration.

References

Alexander, M. J., Beres, J. H., and Pfister, L.: Tropical stratospheric gravity wave activity and relationships to clouds, J. Geophys. Res., 105, 22 299–22 309, 2000.

Alexander, M. J. and Dunkerton, T. J.: A spectral parameterization of mean-flow forcing due to breaking gravity waves, J. Atmos. Sci., 56, 4167–4182, 1999.

Alexander, M. J. and Pfister, L.: Gravity wave momentum flux in the lower stratosphere over convection, Geophys. Res. Lett., 22, 2029–2032, 1995.

Alexander, M. J. and Vincent, R. A.: Gravity waves in the tropical lower stratosphere: A model study of seasonal and interannual variability, J. Geophys. Res., 105, 17 983–17 993, 2000.

Bacmeister, J. T., Eckermann, S. D., Newman, P. A., Lait, L., Chan, K. R., Loewenstein, M., Proffitt, M. H., and Gary, B. L.: Stratospheric horizontal wavenumber spectra of winds, potential temperature, and atmospheric tracers observed by high-altitude aircraft, J. Geophys. Res., 101, 9441–9470, 1996.

Bacmeister, J. T., Schoeberl, M. R., Lait, L. R., Newman, P. A., and Gary, B. L.: Small-scale waves encountered during AASE, Geophys. Res. Lett., 17, 349–352, 1990a.

Bacmeister, J. T., Schoeberl, M. R., Lait, L. R., Newman, P. A., and Gary, B. L.: ER-2 mountain wave encounter over Antarctica: Evidence for blocking, Geophys. Res. Lett., 17, 81–84, 1990b.

Beres, J., Alexander, M. J., and Holton, J. R.: A method of specifying the gravity wave spectrum above convection based on latent heating properties and background wind, J. Atmos. Sci., 61, 324–337, 2004.

Chun, H.-Y., and Baik, J.-J.: Momentum flux by thermally induced internal gravity waves and its approximation for large-scale models, J. Atmos. Sci., 55, 3299–3310, 1998.

Chun, H.-Y. and Baik, J.-J.: An updated parameterization of convectively forced gravity wave drag for use in large-scale models, J. Atmos. Sci., 59, 1006–1017, 2002.

Denning, R. F., Guidero, S. L., Parks, G. S., and Gary, B. L.: Instrument description of the airborne microwave temperature profiler, J. Geophys. Res., 94, 16 757–16 765, 1989.

Eckermann, S. D. and Vincent, R. A.: Falling sphere observations of anisotropic gravity wave motions in the upper stratosphere over Australia, Pure Appl. Geophys., 130, 509–532, 1989.

Fritts, D. C. and Alexander, M. J.: Gravity wave dynamics and effects in the middle atmosphere, Rev. Geophys., 41(1), 1003, doi:10.1029/2001RG000106, 2003.

Gossard, E. E. and Hooke, W. H.: Waves in the Atmosphere, Elsevier Science, New York,

ACPD

5, 11377–11412, 2005

1975.
Haag, W. and Kärcher, B.: The impact of aerosols and gravity waves on cirrus clouds at mid-latitudes, J. Geophys. Res., 109, doi:10.1029/2004JD004579, 2004.
Holton, J. R.: The role of gravity wave induced drag and diffusion in the momentum budget of the mesosphere, J. Atmos. Sci., 39, 791–799, 1982.
Isler, J. R., Taylor, M. J., and Fritts, D. C.: Observational evidence of wave ducting and evanescence in the atmosphere, J. Geophys. Res., 102, 26 301–26 313, 1997.
Jensen, E. J. and Pfister, L.: Transport and freeze-drying in the tropical tropopause layer, J. Geophys. Res., 109, doi:10.1029/2003JD004022, 2004.
Jensen, E. J., Pfister, L., Ackerman, A. S., and Tabazadeh, A.: A conceptual model of the dehydration of air due to freeze-drying by optically thin, laminar cirrus rising slowly across the tropical tropopause, J. Geophys. Res., 106, 17 273–17 252, 2001.
Jensen, E., Pfister, L., Bui, T. P., Weinheimer, A., Weinstock, E., Smith, J., Pittman, J., Baumgardner, D., Lawson, P., and McGill, M. J.: Formation of a tropopause cirrus layer observed over Florida during CRYSTAL-FACE, J. Geophys. Res., 110, doi:10.1029/2004JD004671, 2005.
Jensen, E. J., Starr, D., and Toon, O. B.: Mission investigates tropical cirrus clouds, EOS, 85, 45–50, 2004.
Kraus, J. D.: Radio Astronomy, McGraw-Hill, New York, 1966.
Marks, C. J. and Eckermann, S. D.: A three-dimensional nonhydrostatic ray-tracing model for gravity waves: Formulation and preliminary results for the middle atmosphere, J. Atmos. Sci., 52, 1959–1984, 1995.
McFarlane, N. A.: The effect of Orographically excited gravity wave drag on the general circulation of the lower stratosphere and troposphere, J. Atmos. Sci., 44, 1775–1800, 1987.
Palmer, T. N., Shutts, G. J., and Swinbank, R.: Alleviation of asystematic westerly bias in general circulation and numerical weather prediction models through an orographic gravity wave drag parameterization, Q. J. R. Meteorol. Soc., 112, 1001–1039, 1986.
Pfister, L., Chan, K. R., Bui, T. P., Bowen, S., Legg, M., Gary, B. L., Kelly, K., Proffitt, M., and Starr, W.: Gravity waves generated by a tropical cyclone during the step tropical field program: a case study, J. Geophys. Res., 98, 8611–8638, 1993.
Scott, S. G., Bui, T. P., Chan, K. R., and Bowen, S. W.: The meteorological measurement system on the NASA ER-2 aircraft, J. Atmos. Oceanic Technol., 7, 525–540, 1990.
Solomon, S., Garcia, R. R., Rowland, F. S., and Wuebbles, D. J.: On the depletion of Antarctic

ozone, Nature, 321, 755–758, 1986.
Stockwell, R. G. and Lowe, R. P.: Airglow imaging of gravity waves, 1. Results from a small network of OH nightglow scanning imagers, J. Geophys. Res., 106, 17 185–17 203, 2001.
Stockwell, R. G., Mansinha, L., and Lowe, R. P.: Localisation of the complex spectrum: the S transform, J. Assoc. Expl. Geophys., XVII, 99–114, 1996.
Swenson, G. R., Alexander, M. J., and Haque, R.: Dispersion imposed limits on atmospheric gravity waves in the mesosphere: observations from oh airglow, Geophys. Res. Lett., 27, 875–878, 2000.
Vincent, R. A. and Alexander, M. J.: Gravity waves in the tropical lower stratosphere: An observational study of seasonal and interannual variability, J. Geophys. Res., 105, 17 971–17 982, 2000.
Wang, L.: Gravity wave analysis of four years of high vertical resolution U.S. radiosonde data, PhD thesis, State University of New York at Stony Brook, 2003.
Wang, L., Geller, M. A., and Alexander, M. J.: Spatial and temporal variations of gravity wave parameters, Part I: Intrinsic frequency, wavelength, and vertical propagation direction, J. Atmos. Sci., 62, 125–142, 2005b.
Zink, F. and Vincent, R. A.: Wavelet analysis of stratospheric gravity wave packets over Macquarie Is-land 1. Wave parameters, J. Geophys. Res., 106, 10 275–10 288, 2001.

Table 1. The date, take-off and landing time (UTC) of each ER-2 flight during the CRYSTAL-FACE campaign.

Date	03/07	07/07	09/07	11/07	13/07	16/07	19/07	23/07	26/07	28/07
Take-off	14:36	16:01	15:18	14:59	17:00	18:06	17:02	17:13	15:51	16.56
Landing	20:23	22:39	21:11	21:18	23:09	23:59	23:34	24:18	21:14	23:11

ACPD

5, 11377–11412, 2005

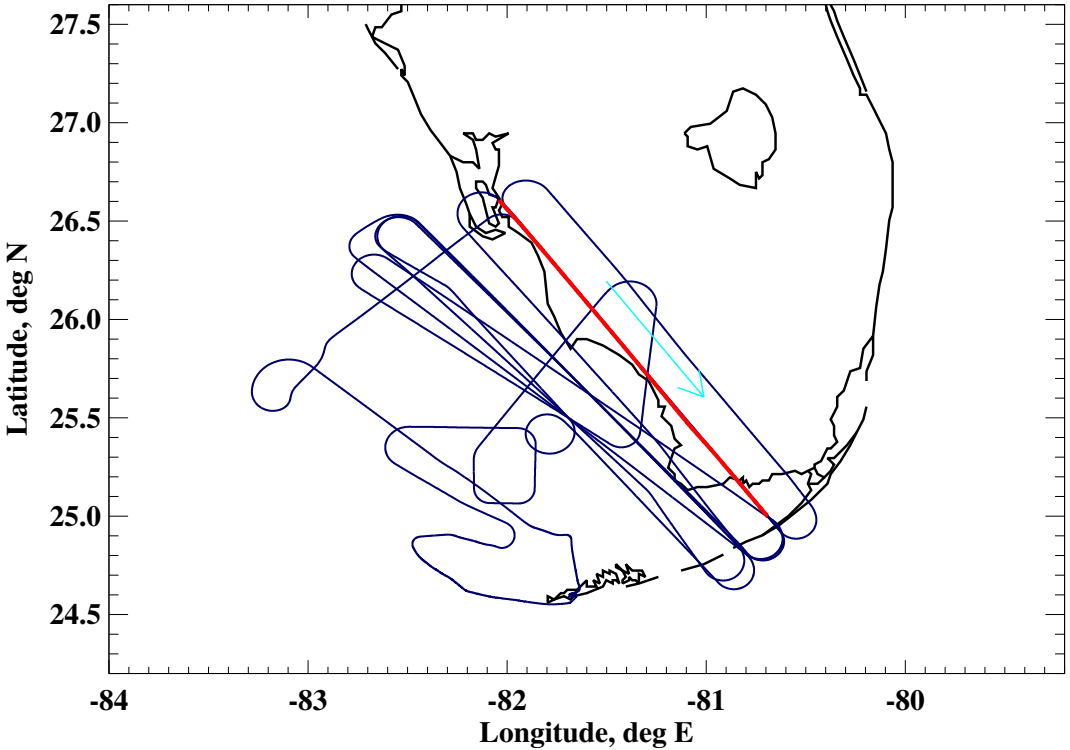

Fig. 1. The ER-2 flight track (blue line) during 7 July 2002 16:01–22:39 UTC. The red line shows the flight segment to be analyzed as an example in this study. The arrow indicates the direction of the flight segment. In total, there were 10 flights from which 136 flight segments were identified. See text for details.

ACPD

5, 11377–11412, 2005

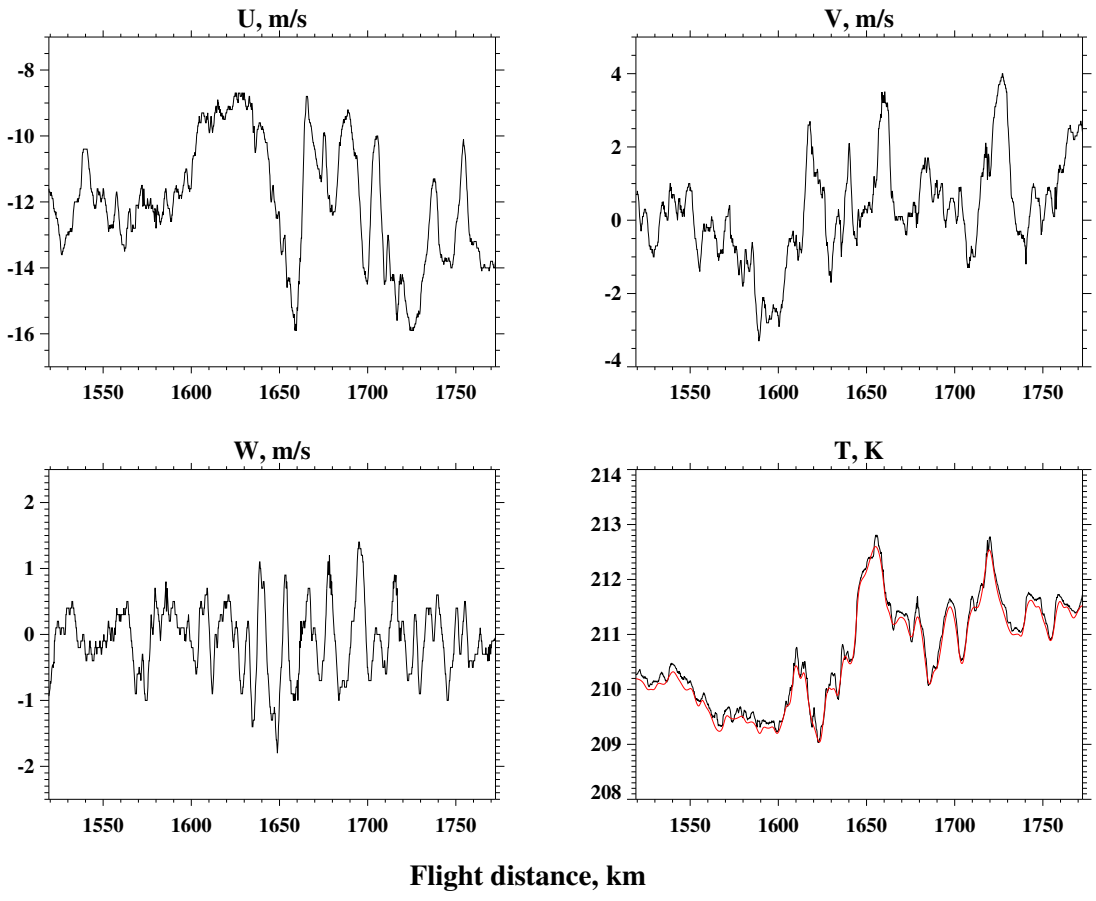

Fig. 2. MMS winds and temperatures (dark lines) as a function of flight distance for the flight segment highlighted in Fig. 1. Also plotted is the MTP temperature at the flight altitude (red line). In this plot, the raw data were interpolated to a regular distance grid with an interval of 0.2 and 2 km for MMS and MTP data, respectively.

ACPD
5, 11377–11412, 2005

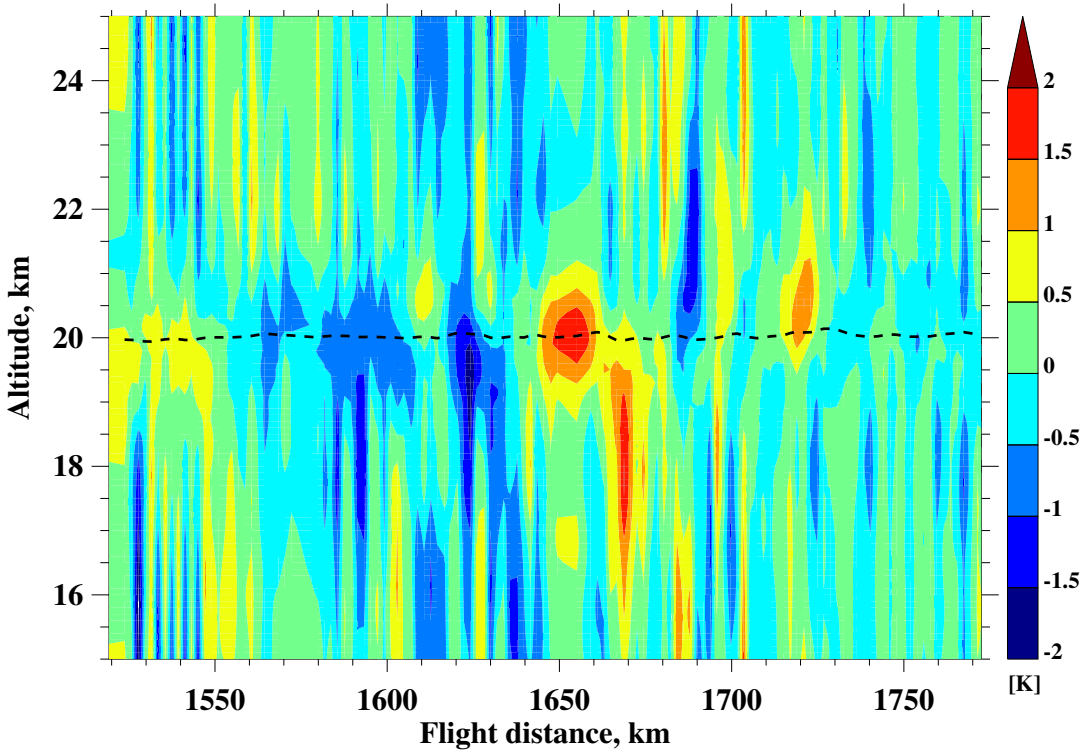

Fig. 3. Contour (flight distance vs. altitude) of the MTP temperature linearly detrended in the vertical for the flight segment highlighted in Fig. 1. The dashed dark line shows the corresponding ER-2 flight altitude. The contour interval is 0.5˚K. See text for details.

ACPD
5, 11377–11412, 2005

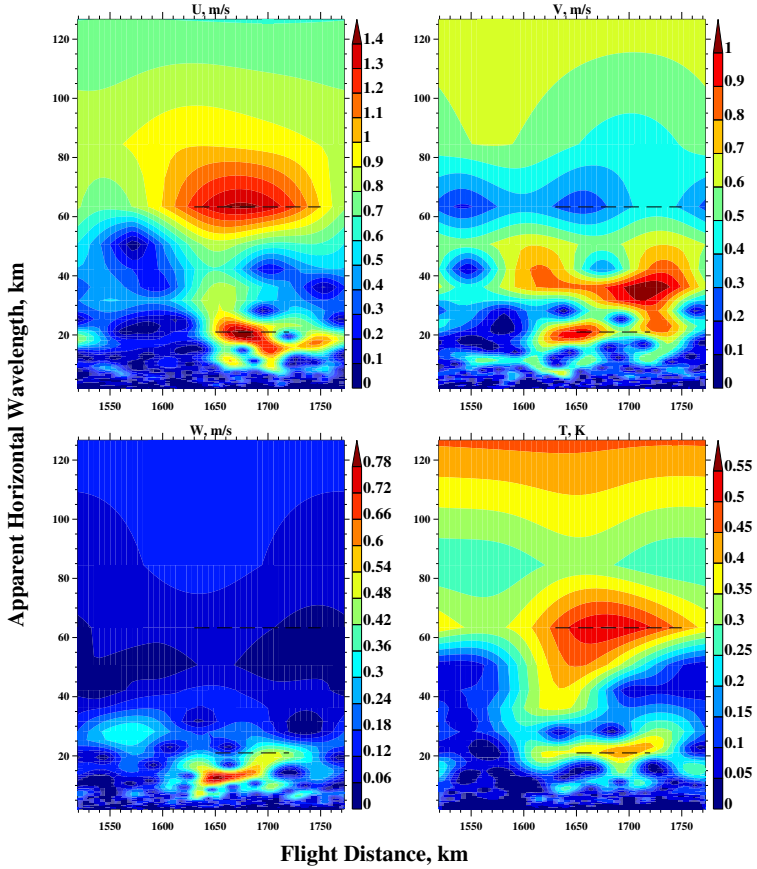

Fig. 4. Contours of horizontal distance vs. apparent horizontal wavelength λ'_h of wave amplitudes of winds and temperatures from the S-transform for the regularly gridded MMS data shown in Fig. 2. The contour interval is 0.1 ms^{-1} for zonal and meridional winds, 0.06 ms^{-1} for vertical wind, and 0.05°K for temperature.

ACPD
5, 11377–11412, 2005

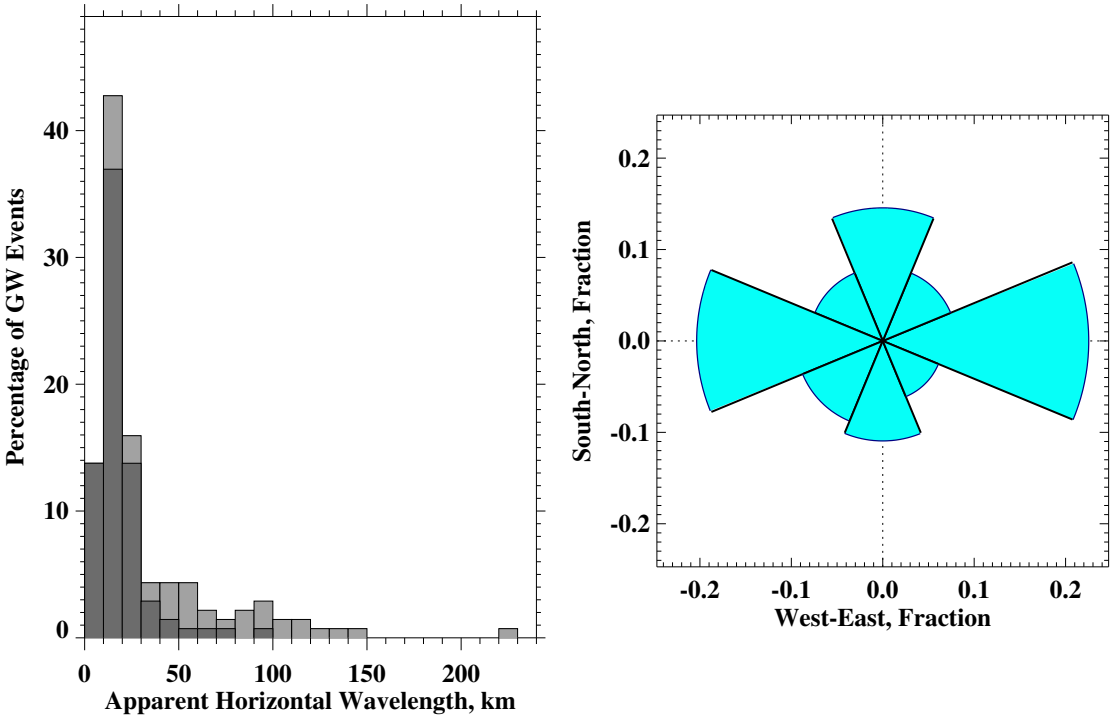

Fig. 5. Histogram (in percentage) of apparent horizontal wavelengths λ_h' for the 138 GW events identified (left panel) and angular distribution of flight directions of the events (right panel). The dark histogram in the left panel includes only those events which had large wave amplitudes in both w and T. See text for details.

ACPD
5, 11377–11412, 2005

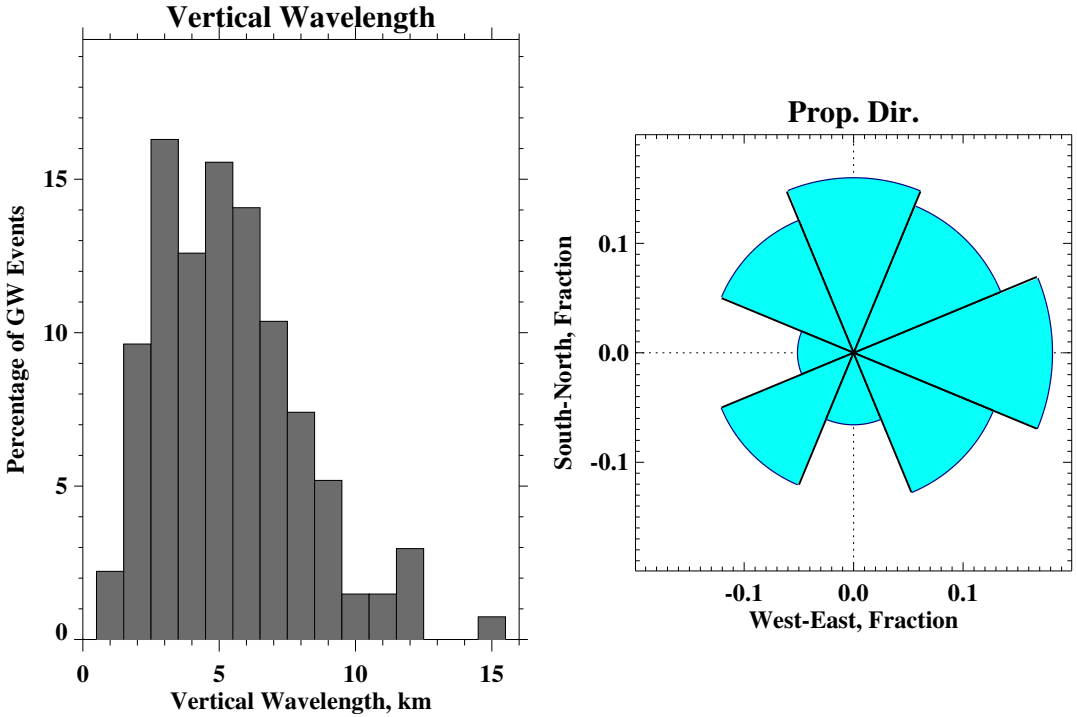

Fig. 6. Histogram (in percentage) of vertical wavelengths λ_z, and the angular distribution of horizontal propagation directions ϕ for the GW events identified. Note that 138 events were included in the plot for ϕ, whereas 135 were included for λ_z. See text for details.

ACPD
5, 11377–11412, 2005

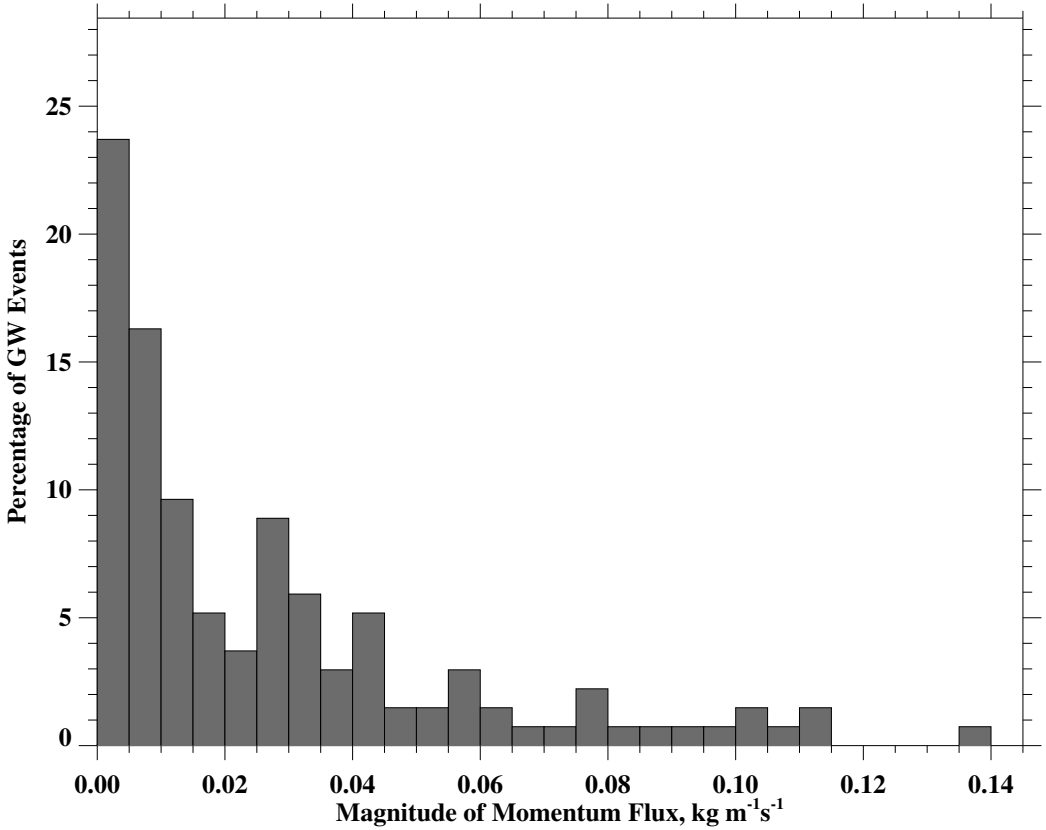

Fig. 7. Histogram (in percentage) of magnitudes of momentum flux (kg m^{-1} s^{-1}) for all the 138 events identified. See text for details.

ACPD

5, 11377–11412, 2005

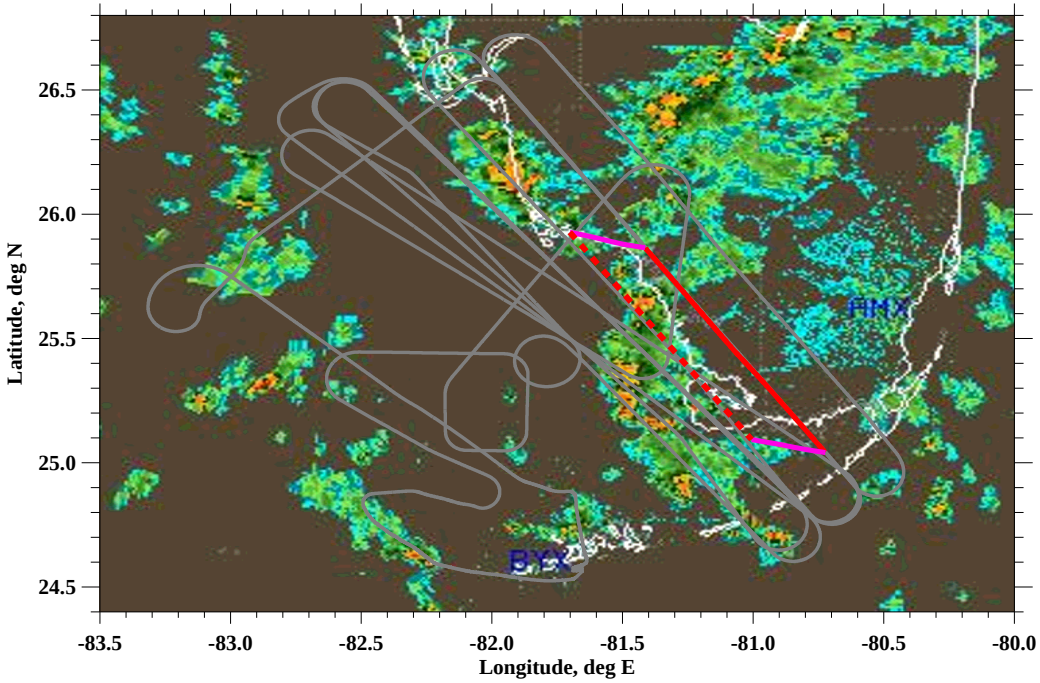

Fig. 8. The NEXRAD radar reflectivity image on 7 July 2002 17:20 UTC. The thin gray line is the ER-2 flight track on that day. The solid red line denotes the GW event with the longer λ'_h at ~18:20 UTC, as shown in Fig. 4. The pink lines denote the trajectories at both ends of the event reversely ray-traced 1 h back to 17:20 UTC. The dotted red line connects the end points of the trajectories and indicates where the wave event could have been 1 h earlier. See text for details.

ACPD
5, 11377–11412, 2005

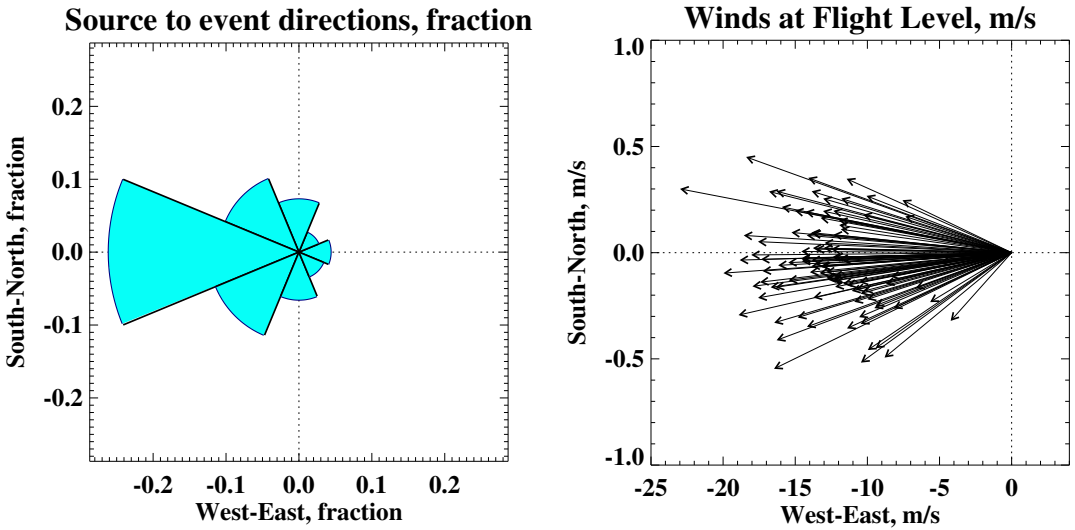

Fig. 9. Angular distribution of source to event directions for those events related to convective sources (102 in total), and the scatter plot of their background winds at flight level (~20 km).

ACPD
5, 11377–11412, 2005

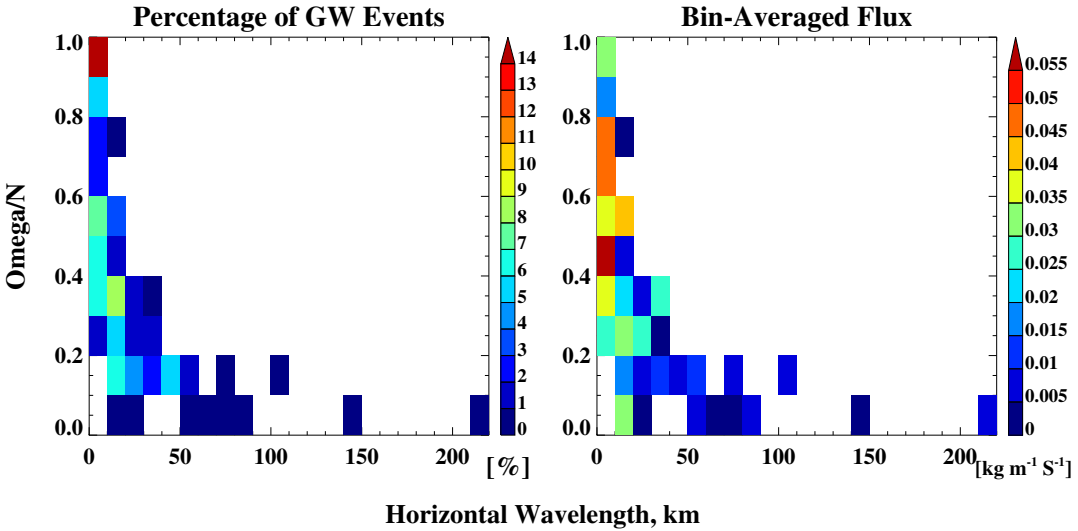

Fig. 10. Percentages of GW events within λ_h and $\hat{\omega}/N$ bins (left panel), and bin-averaged momentum flux magnitudes (kg m^{-1} s^{-1}) (right panel). See text for details.

ACPD
5, 11377–11412, 2005

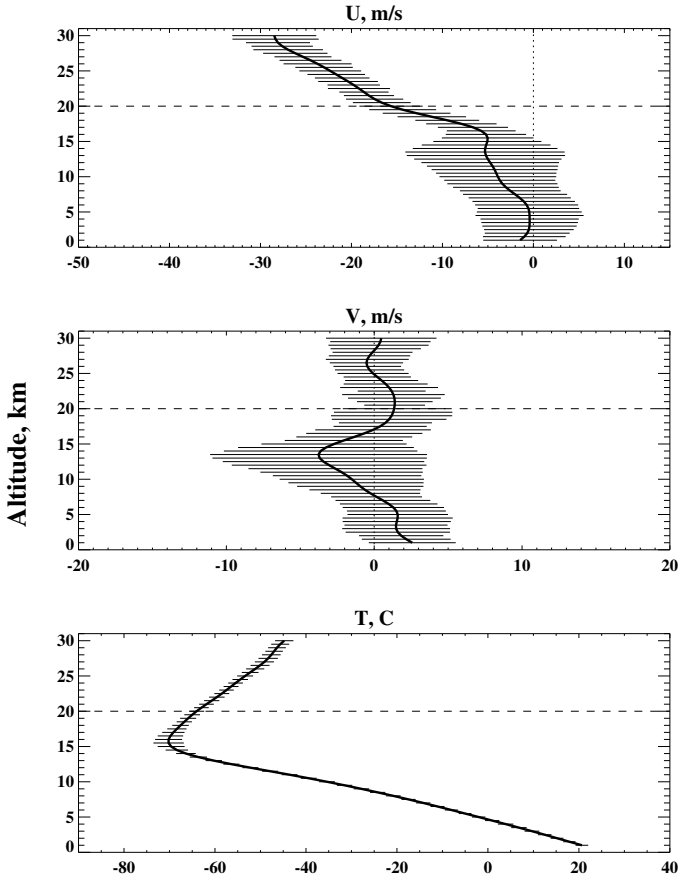

Fig. 11. Typical background winds and temperatures binned from 3–5 times daily high vertical resolution radiosonde observations conducted over the south Florida during the CRYSTAL-FACE campaign. Each error bar is the standard deviation of each bin. The mean flight altitude (20 km) is marked by a thin dashed line in each plot. See text for details.

ACPD
5, 11377–11412, 2005

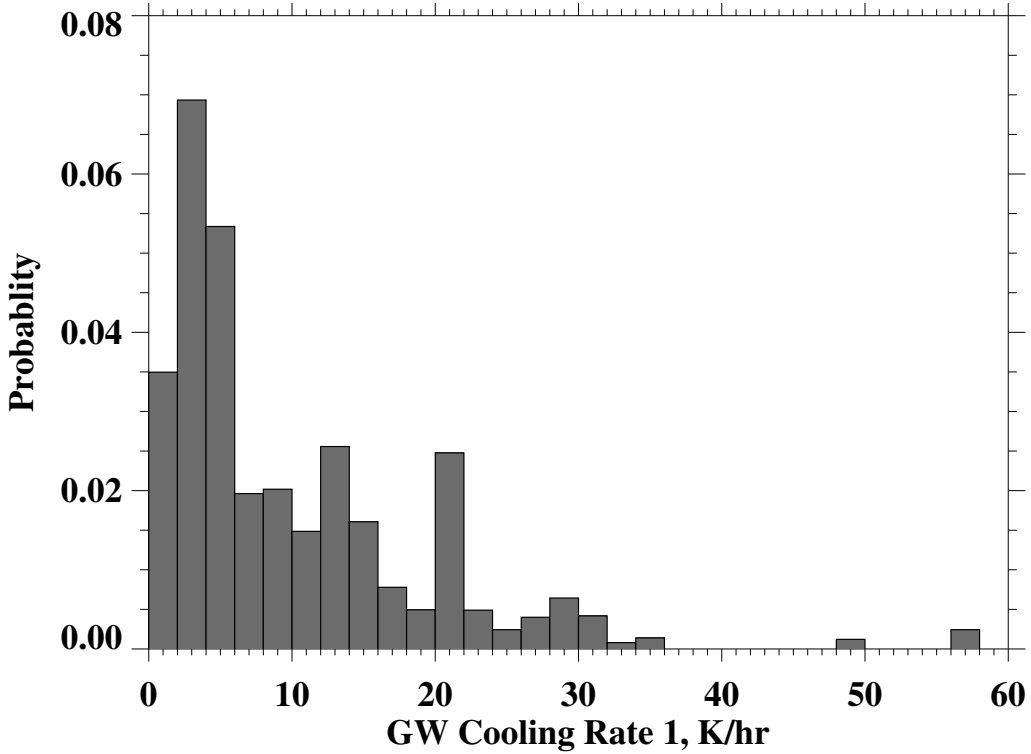

Fig. 12. The probability of observing a GW event with a cooling rate within a given range from the ER-2 aircraft during CRYSTAL-FACE. See text for details.

ACPD
5, 11377–11412, 2005